

Data-constrained fault zone structure improves 0-3 Hz deterministic ground motion predictions for the 2019 M7.1 Ridgecrest earthquake

Te-Yang Yeh and Kim Bak Olsen

Department of Geological Sciences, San Diego State University

Poster #226



SAN DIEGO STATE UNIVERSITY
Department of Geological Sciences
College of Sciences

SC/EC
AN NSF+USGS CENTER

This research was supported by the Southern California Earthquake Center (Contribution No.20157 and 21111). SCEC is funded by NSF Cooperative Agreement EAR-1600087 and USGS Cooperative Agreement G17AC0047.

An award of computer time was provided by the INCITE program. This research used resources of the Oak Ridge Leadership Computing Facility, which is a DOE Office of Science User Facility supported under Contract DE-AC05-00OR22725.

Objectives

- Examining the significance of the fault zone structure for deterministic numerical simulations
- Quantifying the fault zone effects on ground motions, near the source and the regions far away from the source
- Better prediction of ground motions for the densely populated areas (e.g., greater Los Angeles area)

1. Numerical modeling

- Simulations carried out on OLCF Summit using the simulation code AWP
- Domain size: 200 km (W) x 300 km (L) x 150 km (Z)
- USGS Southern California 3-arc-second DEM
- Minimum grid spacing: 15m
- Minimum V_s : 300 m/s
- Maximum frequency: 3Hz
- Kinematic source rupture model from joint seismic and geodetic inversion by Liu *et al.* (2019)
- Velocity model: SCEC UCVM CVM-S4.26.M01
- High-resolution fault zone (FZ) model (to 5 km depth) by Zhou *et al.* (2022)
- Geotechnical layer (GTL) using Ely *et al.* (2010)'s formulation with 700 m tapering depth
- Vs30 model from Wills *et al.* (2015)
- Calibrated anelastic attenuation model:

$$Q_s = 0.1V_s \text{ for } f \leq 1\text{Hz}$$

$$Q_s(f) = 0.1V_s f^{0.5} \text{ for } f > 1\text{Hz}$$

$$Q_p = 2Q_s$$

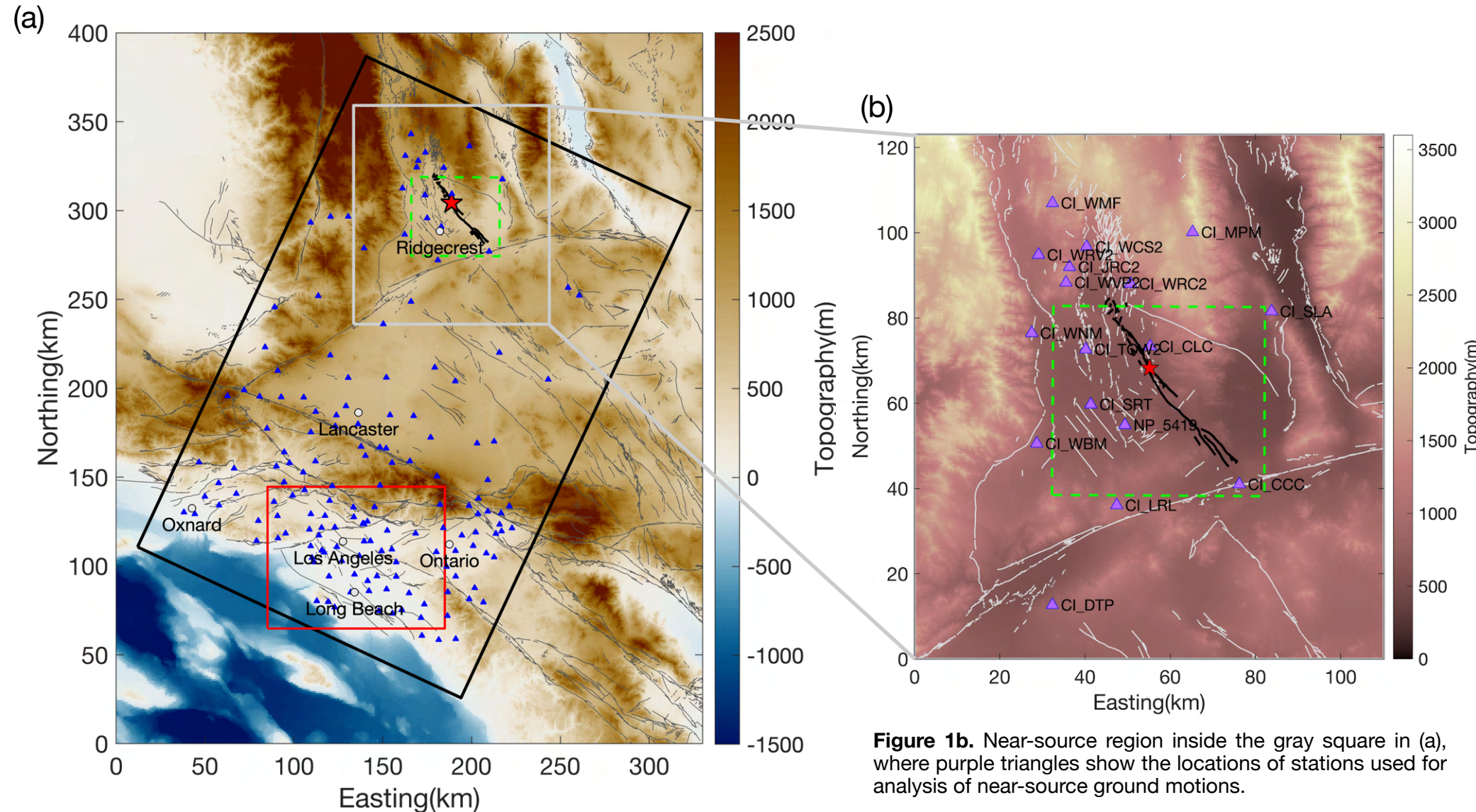


Figure 1a. Model domain (black rectangle) for the simulations. Blue triangles show locations of stations providing seismic recordings of the 2019 Ridgecrest Mw 7.1 earthquake. The green dashed box depicts the domain where the fault zone structure was imaged by Zhou *et al.* (2022). Thick black traces are faults that ruptured in the 2019 Mw 7.1 Ridgecrest earthquake. Red box is where basin amplification is analyzed.

2. Velocity model model

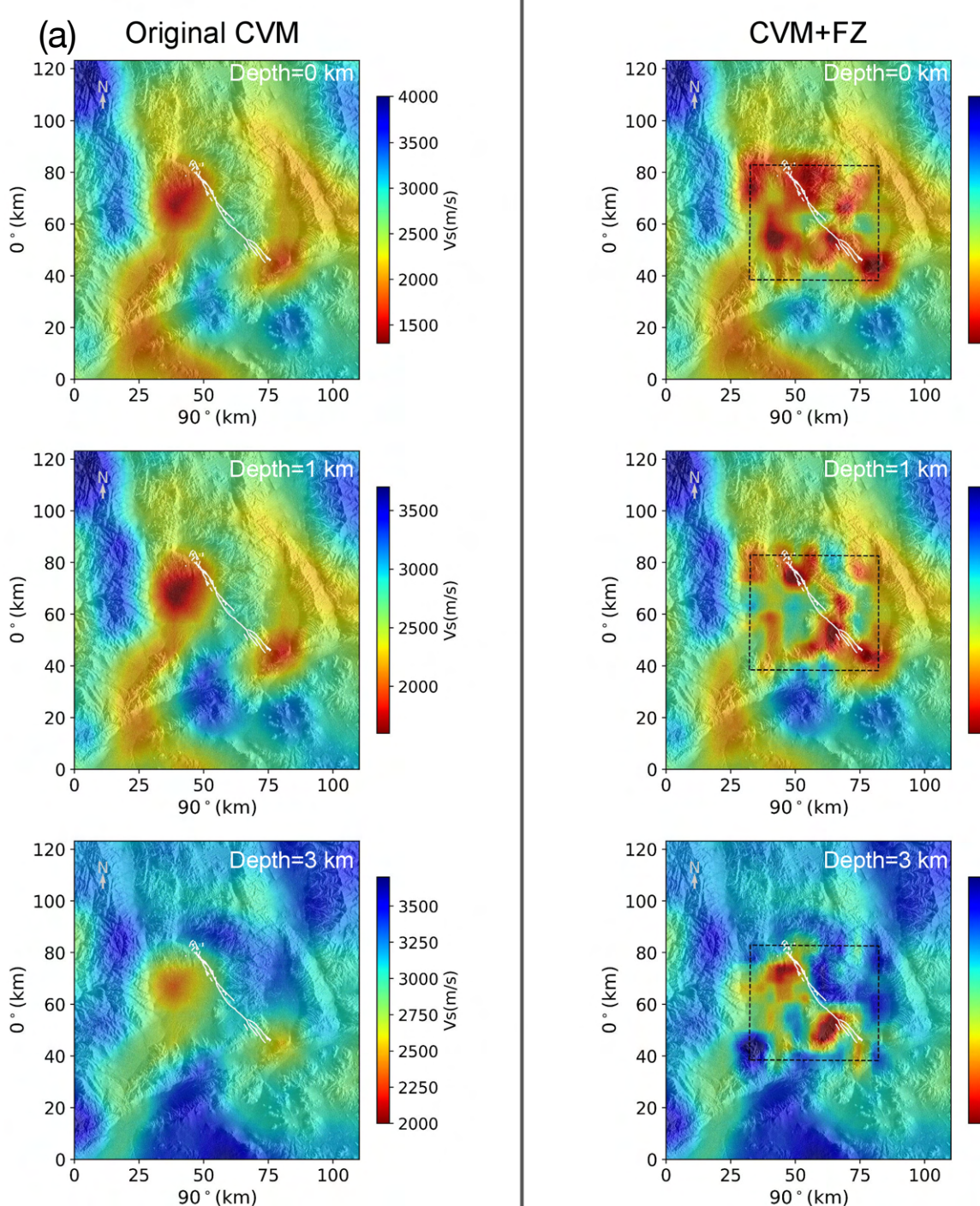


Figure 2a. Comparison of horizontal V_s slices inside the near-source region (Figure 1b) at different depths without (left column) and with (right column) incorporating the fault zone structure. The black dashed box depicts the imaging domain of the fault zone model. Note that the slices do not include the GTL.

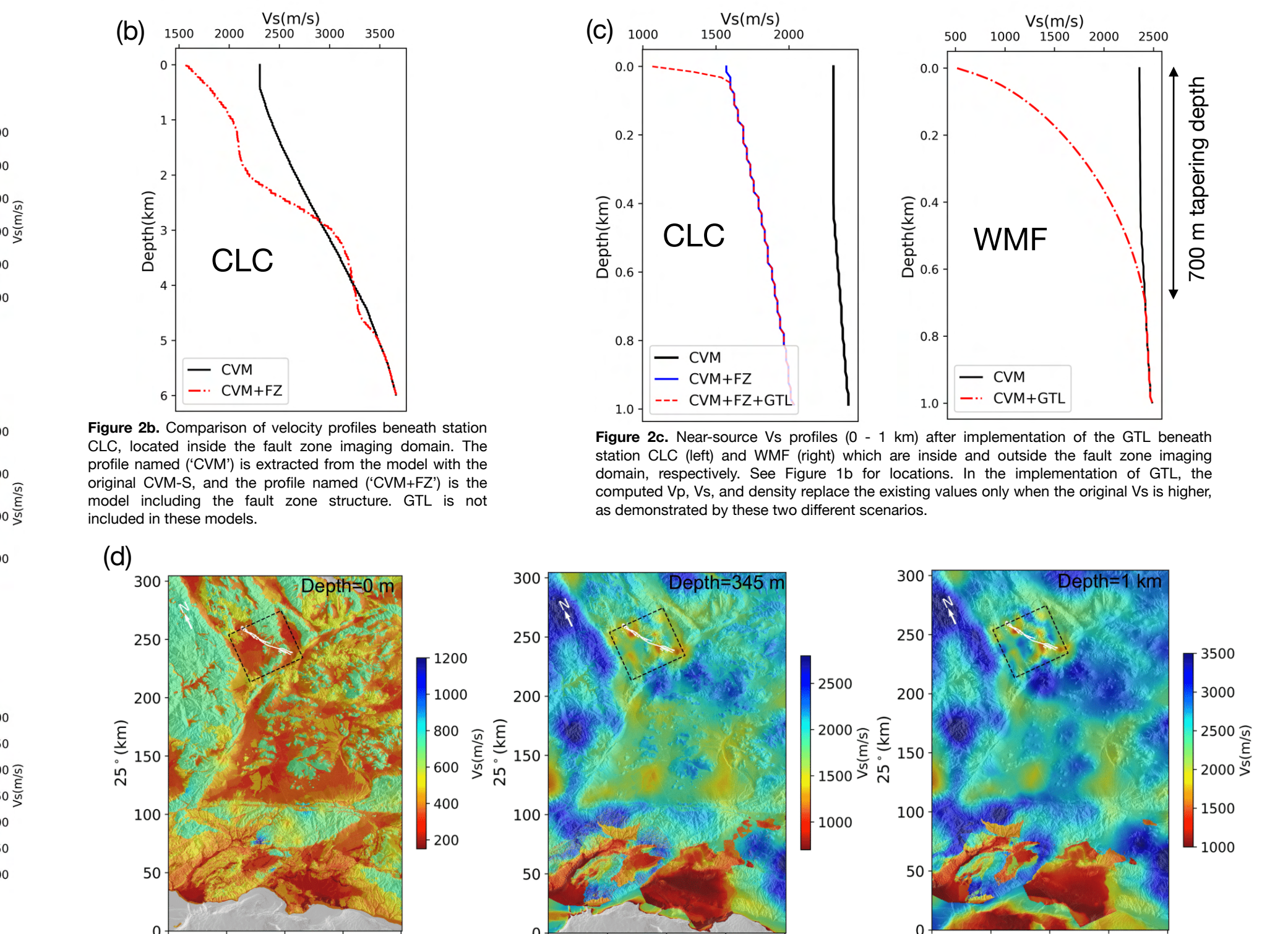


Figure 2b. V_s slices in the modeling domain (black box in Figure 1a) at different depths, including the fault zone structure and the GTL (CVM+FZ+GTL). The black dashed box depicts the imaging domain of the fault zone.

3. Fault zone effects (near-fault)

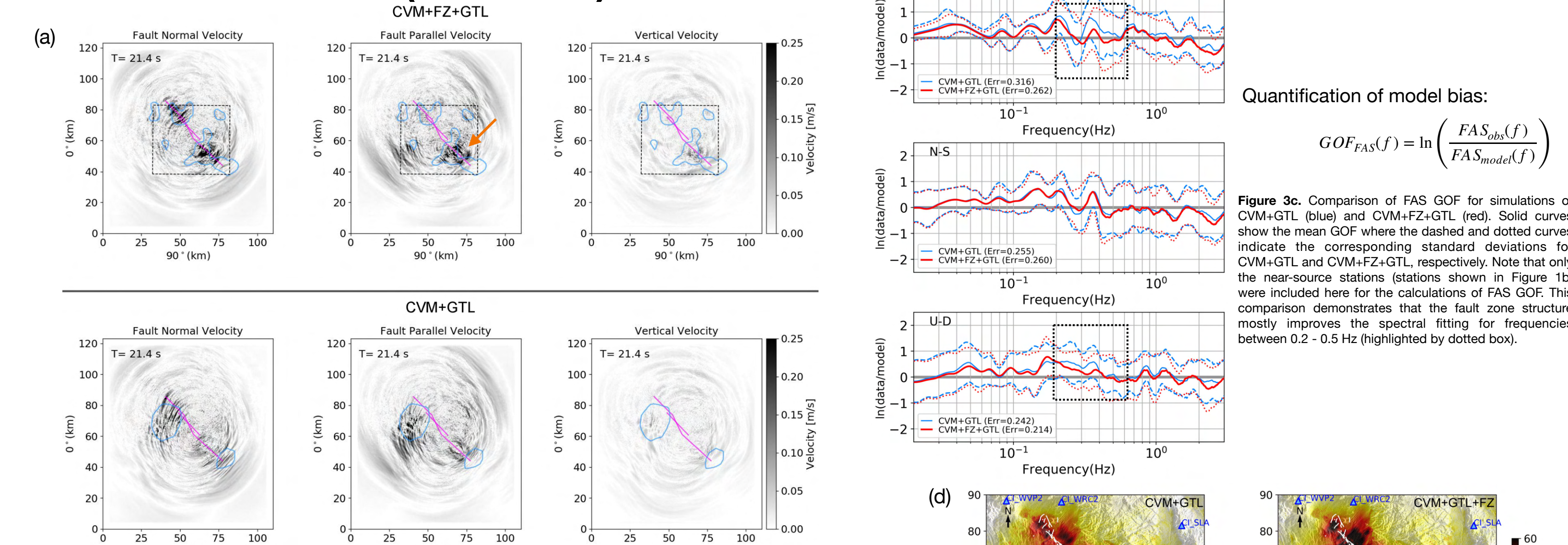


Figure 3a. Snapshots of absolute particle velocity along (left column) fault normal, (center column) fault parallel and (right column) vertical directions in the near-fault region (Figure 1b) for simulations with (top) CVM+FZ+GTL and (bottom) CVM+GTL. The magenta lines depict the fault trace used for simulating the M7.1 Ridgecrest event. The blue curves depict contour lines of $V_s = 210$ m/s at 1 km below free surface in the corresponding models. Orange arrow points out where particle motions are amplified by the near-fault low-velocity materials in the fault zone structure, which initiate the strong Love waves observed in the south around the Los Angeles basin (Figure 4c).

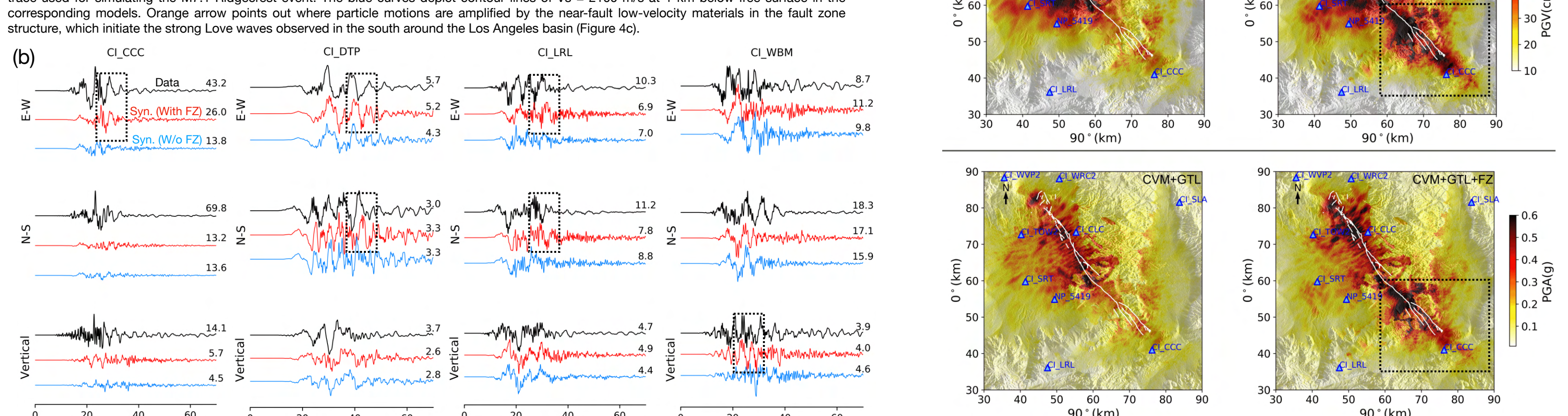


Figure 3b. Comparison of observed and synthetic waveforms computed with and without the fault zone structure at four sites that are close to faults. Black dotted boxes highlight the long-period waves generated by the fault zone structure, in agreement with data.

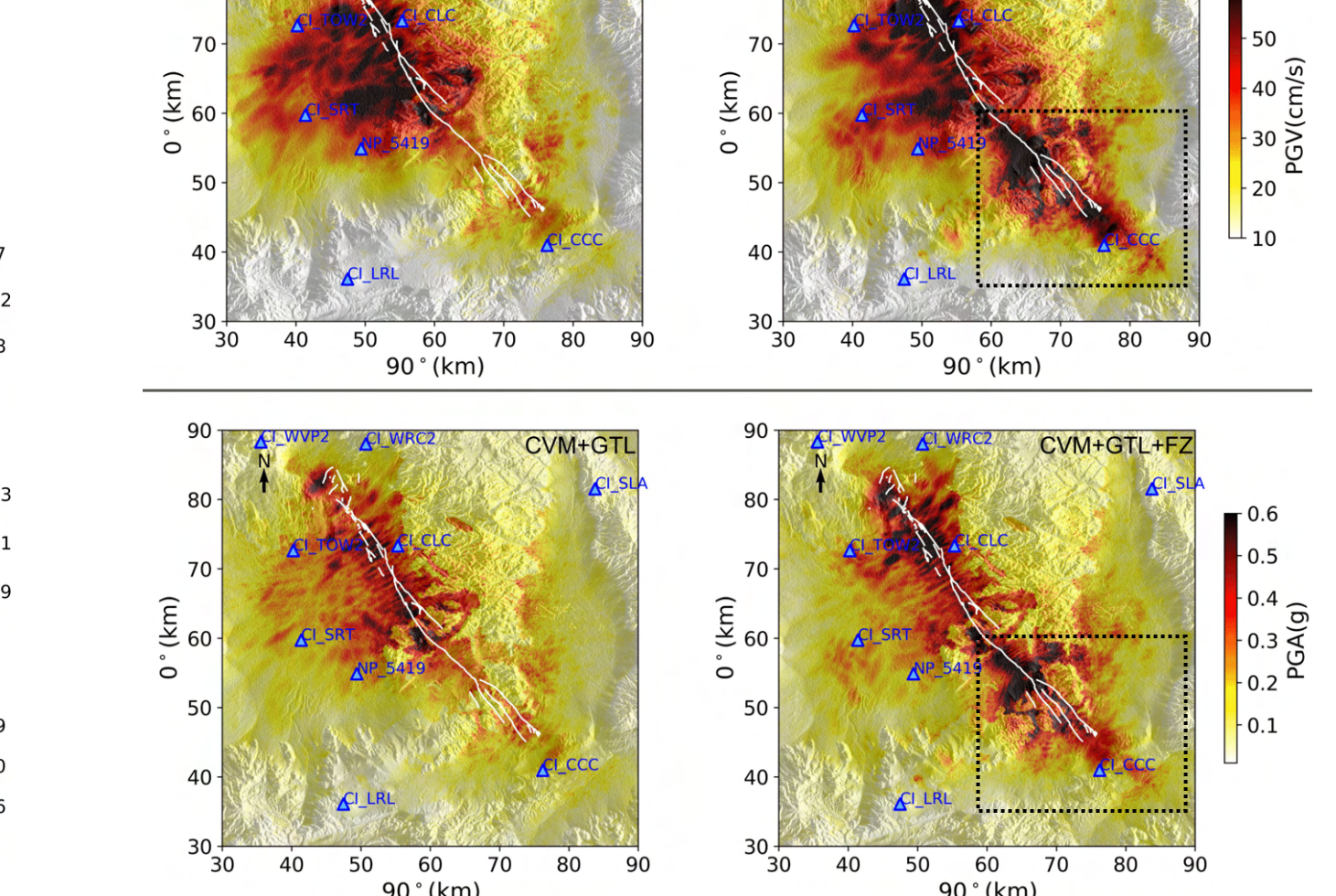


Figure 3c. Peak-ground velocity (top row) and peak-ground acceleration (bottom row) maps computed for CVM+GTL (left panels) and CVM+FZ+GTL (right panels). Black dotted box indicate the region with elevated ground motions due to near-fault low-velocity materials in the fault zone model.

4. Fault zone effects (longer distances)

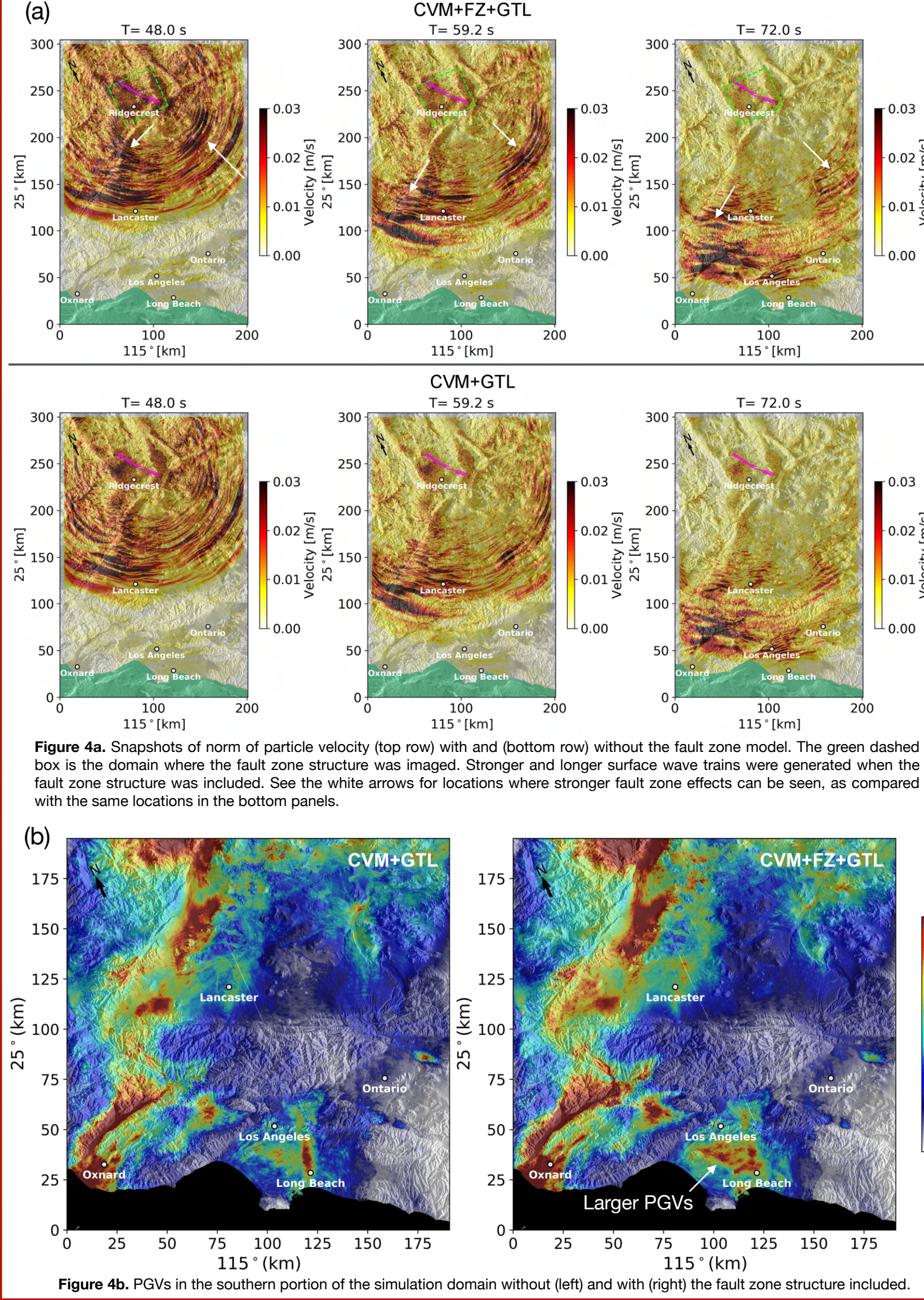


Figure 4a. Snapshots of norm of particle velocity (top row) with and (bottom row) without the fault zone model. The green dashed box is the domain where the fault zone structure was imaged. Stronger and longer surface wave trains were generated when the fault zone structure was included. See the white arrows for locations where stronger fault zone effects can be seen, as compared with the same locations in the bottom panels.

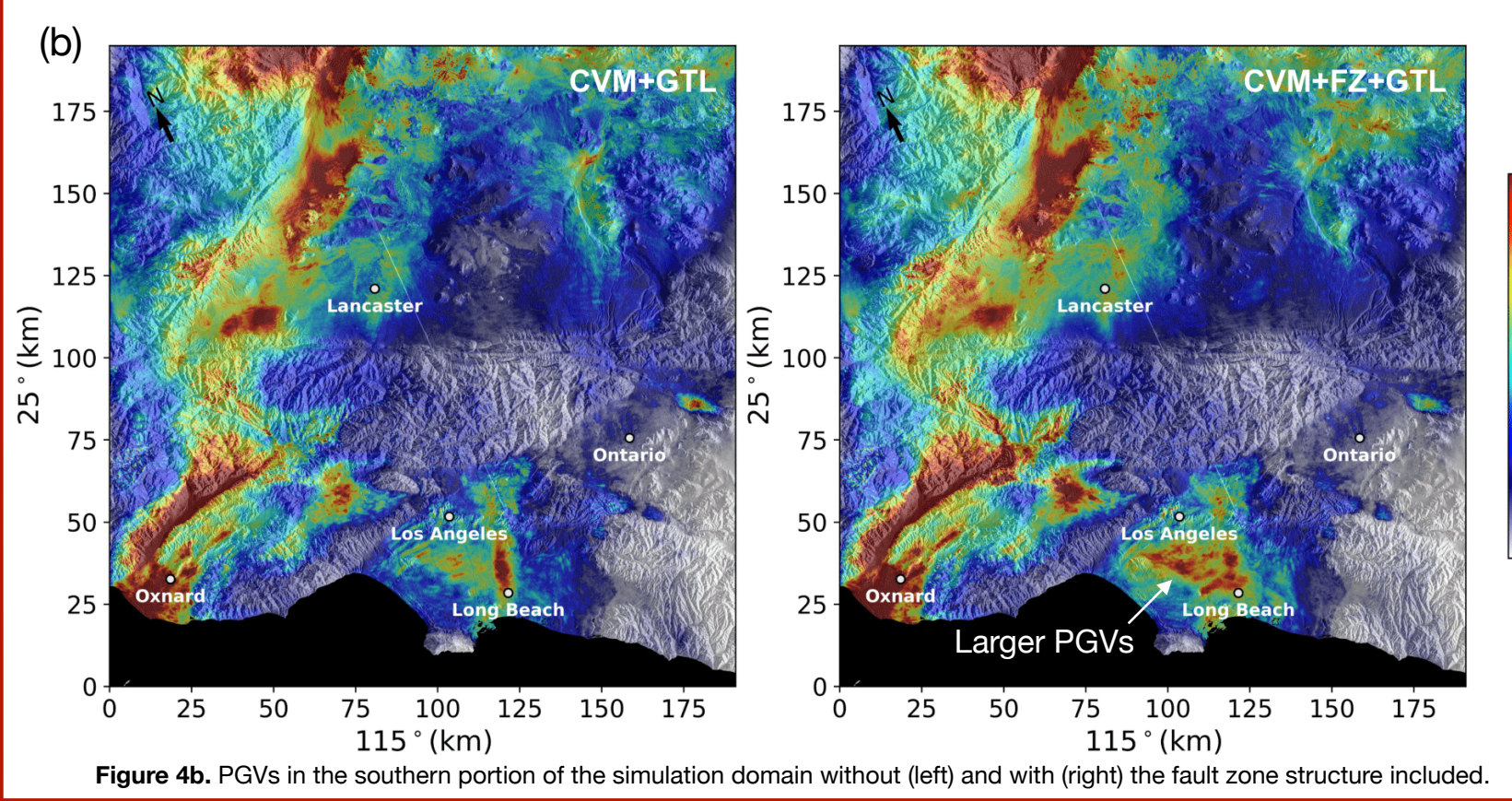


Figure 4b. PGVs in the southern portion of the simulation domain without (left) and with (right) the fault zone structure included.

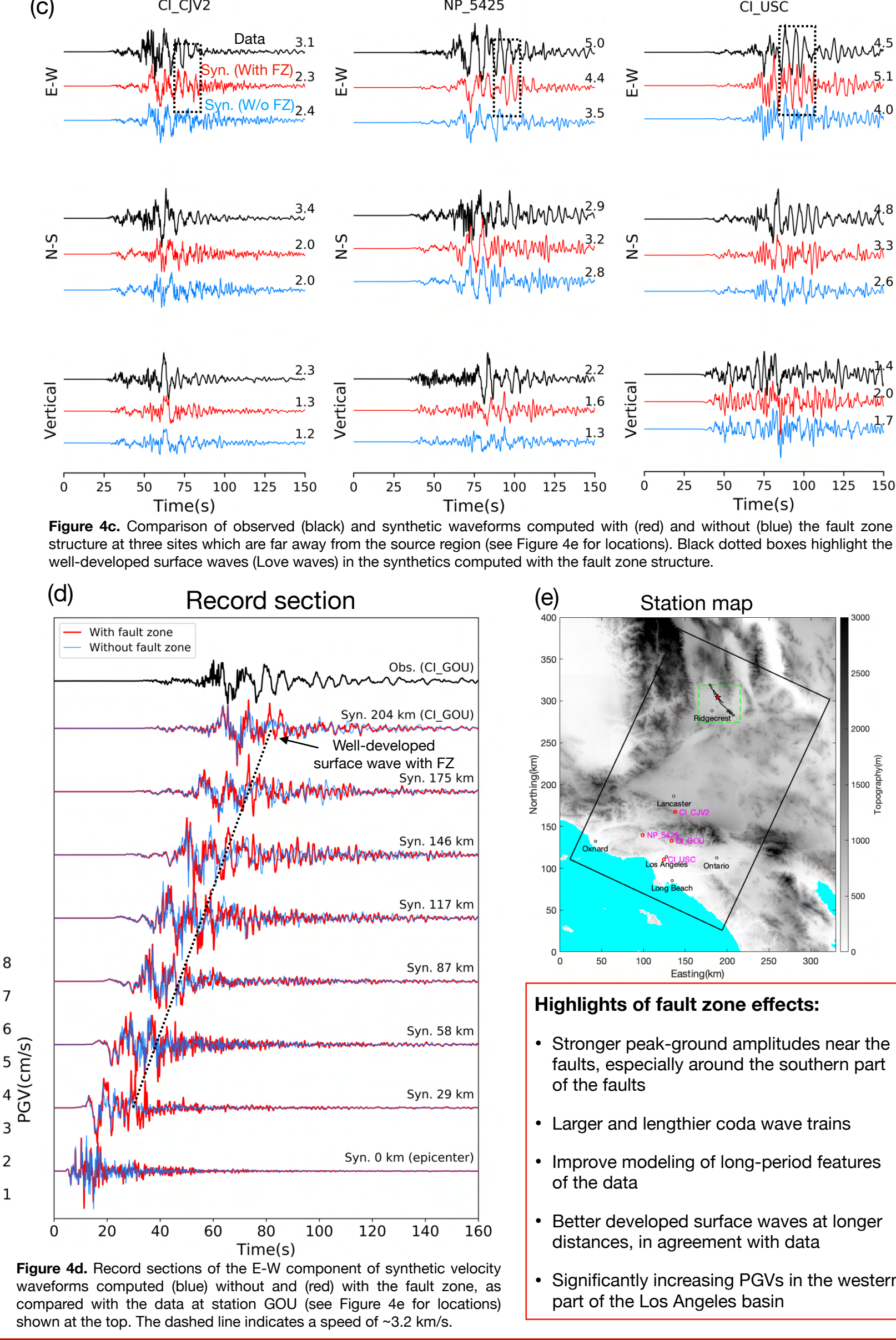


Figure 4c. Comparison of observed (black) and synthetic waveforms computed with (red) and without (blue) the fault zone structure at three sites which are far away from the source region (see Figure 4e for locations). Black dotted boxes highlight the well-developed surface waves (Love waves) in the synthetics computed with the fault zone structure.

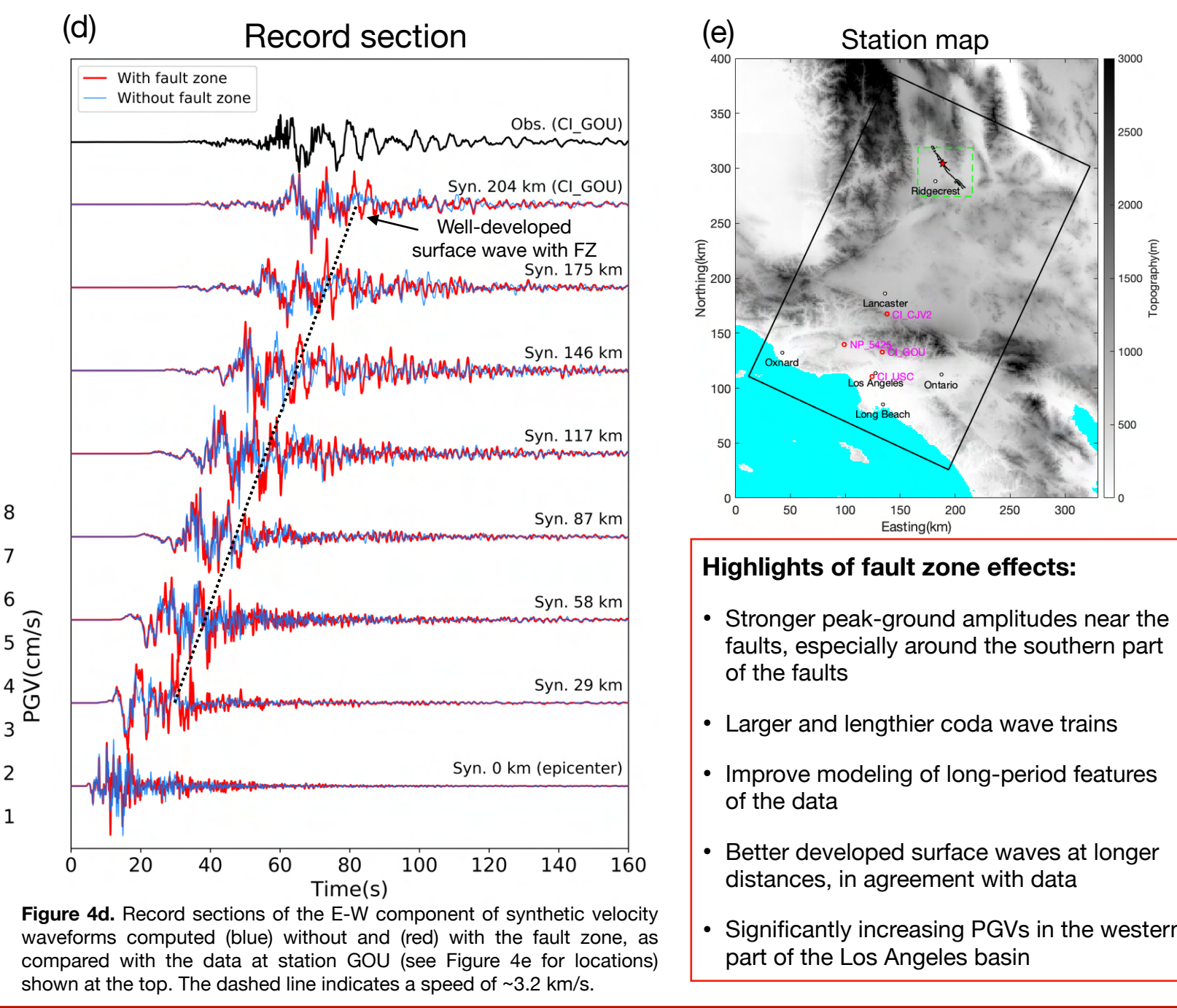


Figure 4d. Record sections of the E-W component of synthetic waveforms computed (blue) without and (red) with the fault zone, as compared with the data at station GOU (see Figure 4e for locations) shown at the top. The dashed line indicates a speed of ~ 3.2 km/s.

- Highlights of fault zone effects:**
- Stronger peak-around the southern part of the faults
 - Larger and lengthier coda wave trains
 - Improve modeling of long-period features of the data
 - Better developed surface waves at longer distances, in agreement with data
 - Significantly increasing PGVs in the western part of the Los Angeles basin

5. Basin amplification

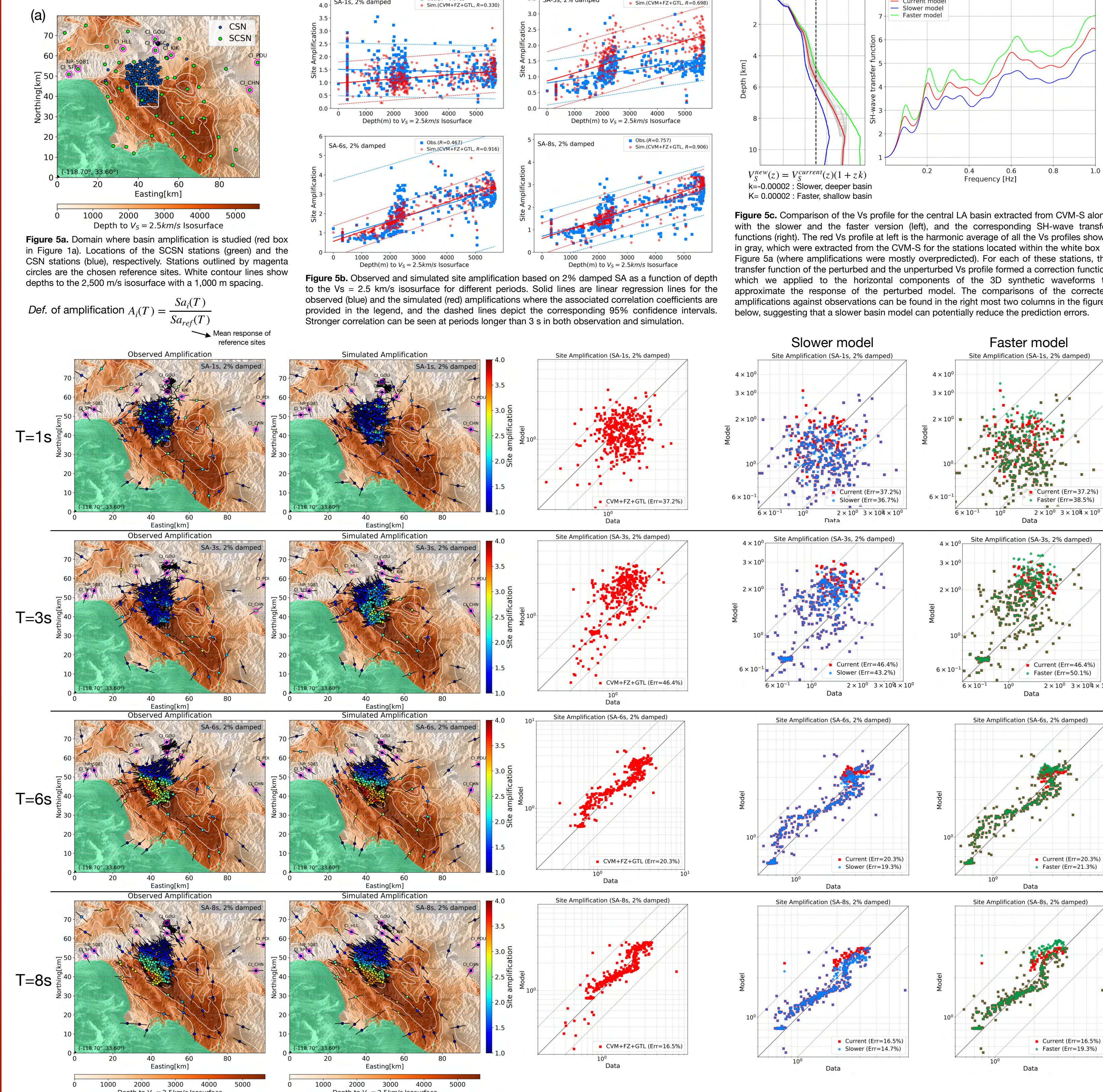


Figure 5a. Domain where basin amplification is studied (red box in Figure 1a). Locations of the SCSEN stations (green) and the CSN stations (blue), respectively. Stations outlined by magenta circles are the chosen reference sites. White contour lines show depths to the 2,500 m/s isosurface with a 1,000 m spacing.

Def. of amplification $A_s(T) = \frac{S_a(T)}{S_{a,ref}(T)}$

Mean response of reference sites

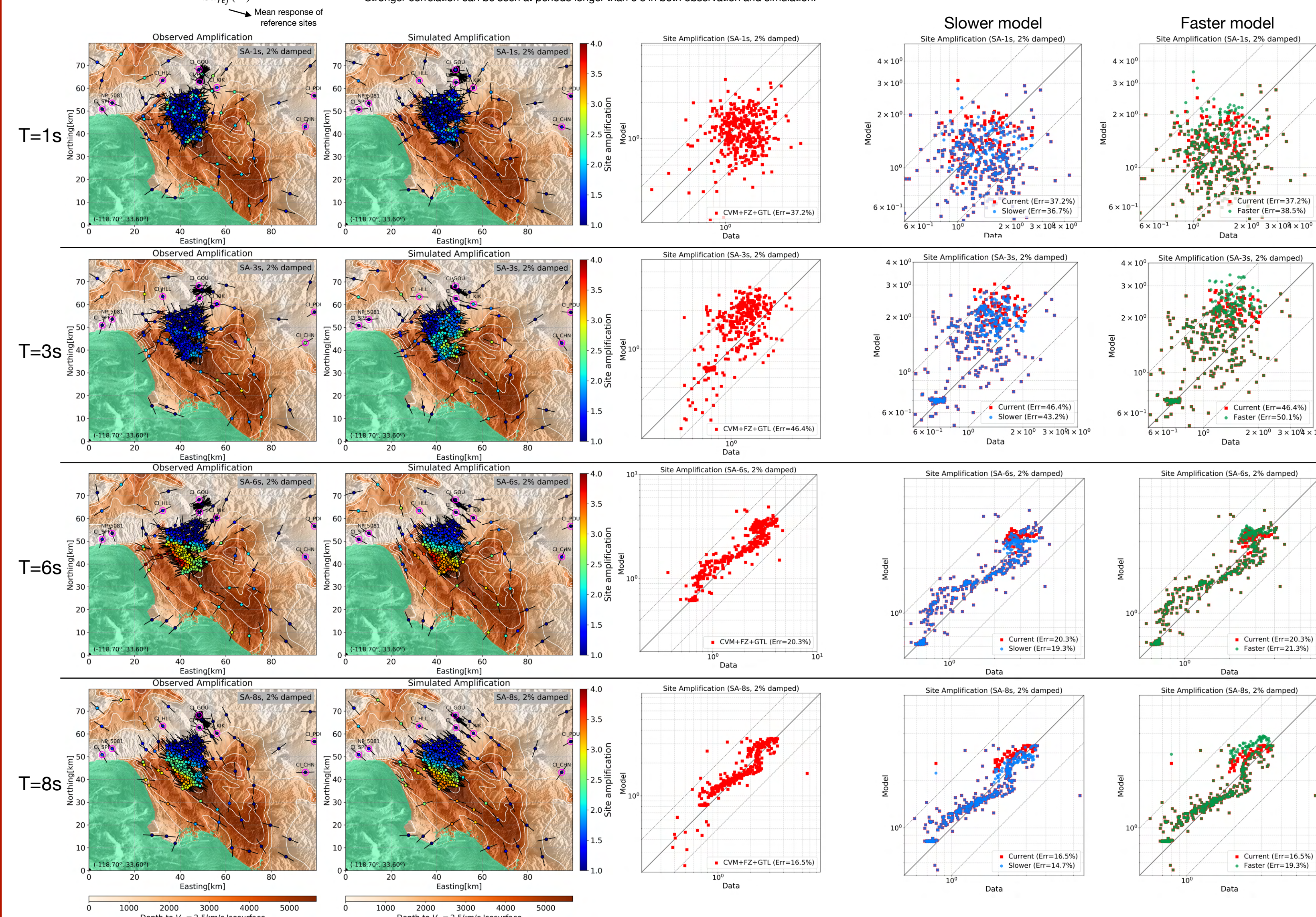


Figure 5b. Observed and simulated site amplification based on 2% damped SA as a function of depth to the $V_s = 2.5$ km/s isosurface for different periods. Solid lines are linear regression lines for the observed (blue) and the simulated (red) amplifications where the associated correlation coefficients are provided in the legend, and the dashed lines depict the corresponding 95% confidence intervals. Stronger correlation can be seen at periods longer than 3 s in both observation and simulation.

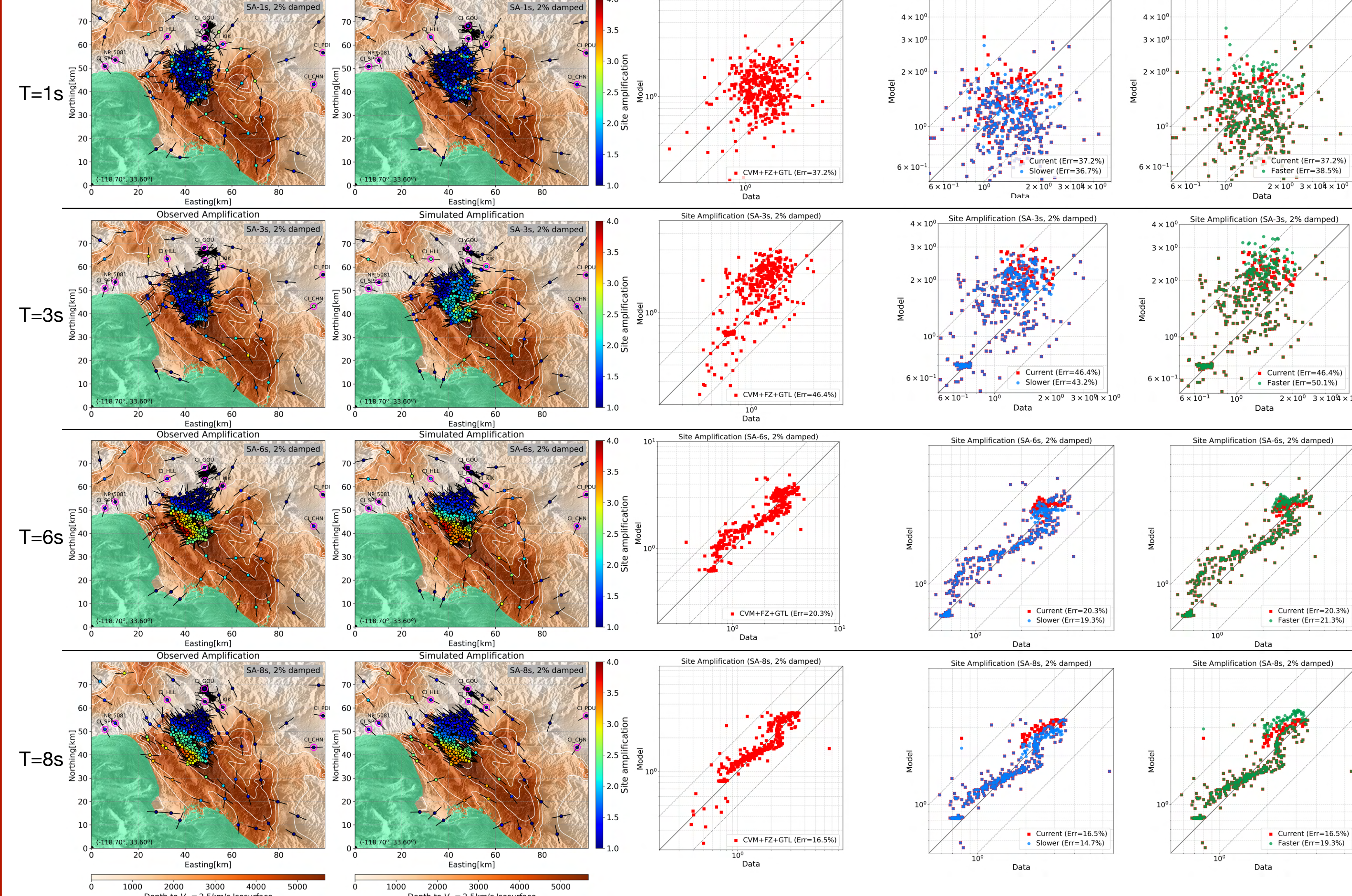


Figure 5c. Comparison of the V_s profile for the central LA basin extracted from CVM-S along with the slower and the faster version (left), and the corresponding SH-wave transfer functions (right). The red V_s profile at left is the harmonic average of all the V_s profiles shown in gray, which were extracted from the CVM-S for the stations located within the white box in Figure 5a (where amplifications were mostly over-predicted). For each of these stations, the transfer function of the perturbed and the unperturbed V_s profile formed a correction function which we applied to the horizontal components of the 3D synthetic waveforms to approximate the response of the perturbed model. The comparisons of the corrected amplifications against observations can be found in the right most two columns in the figures below, suggesting that a slower basin model can potentially reduce the prediction errors.